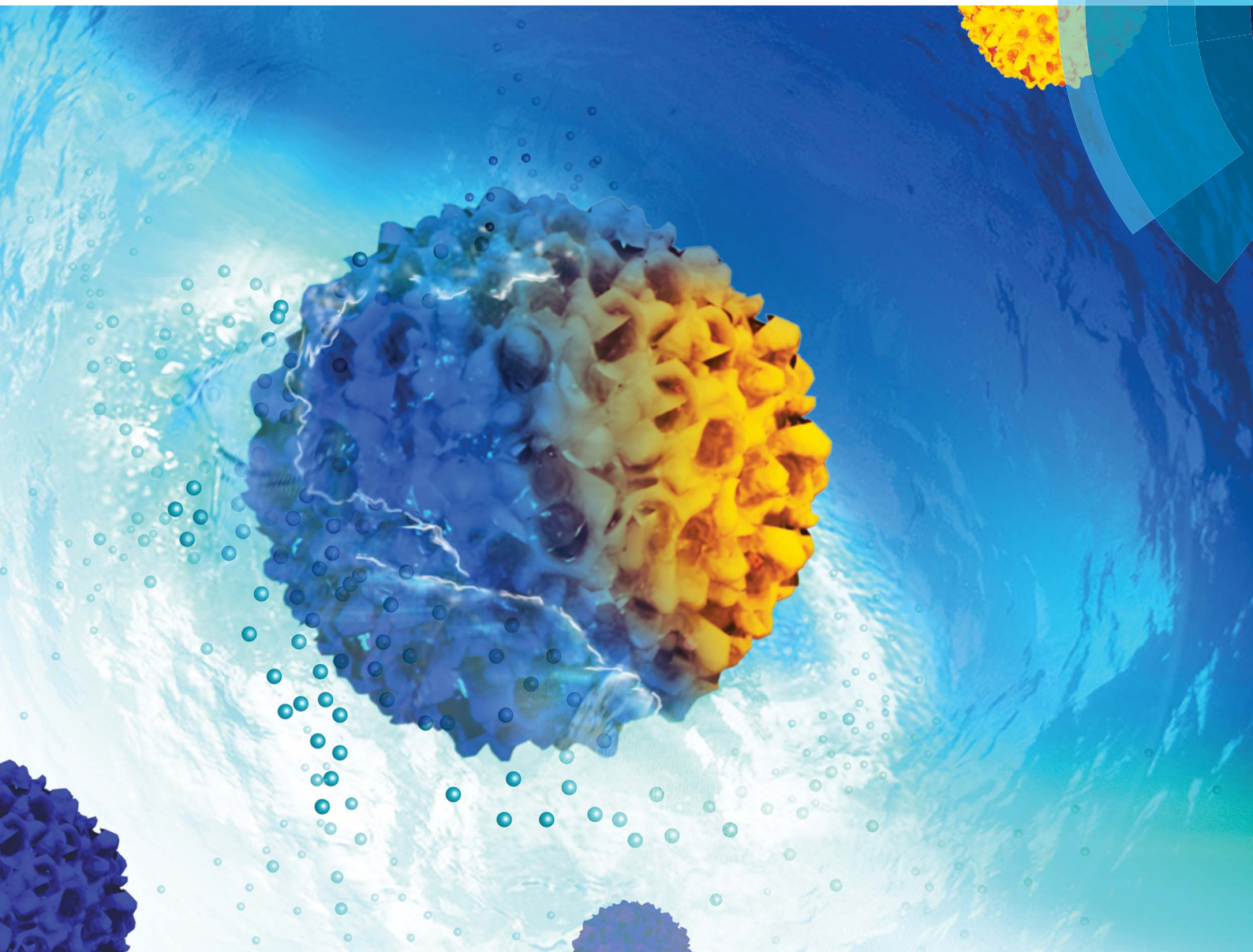


Journal of Materials Chemistry A

Materials for energy and sustainability

www.rsc.org/MaterialsA



ISSN 2050-7488



PAPER

Wancheng Zhu, Qiang Zhang *et al.*
Ionothermal confined self-organization for hierarchical porous
magnesium borate superstructures as highly efficient adsorbents
for dye removal

Cite this: *J. Mater. Chem. A*, 2014, 2, 19167

Ionothermal confined self-organization for hierarchical porous magnesium borate superstructures as highly efficient adsorbents for dye removal†

Zhaoqiang Zhang,^a Wancheng Zhu,^{*a} Ruguo Wang,^a Linlin Zhang,^a Lin Zhu^a and Qiang Zhang^{*b}

Three-dimensional (3D) hierarchical porous structures self-organized by one-dimensional (1D) building blocks have attracted considerable attention due to their unique properties and versatile applications. Herein, uniform hierarchical porous MgBO₂(OH) superstructures with a microsphere-like profile were synthesized for the first time *via* a facile ionothermal synthesis (150 °C, 12.0 h) using MgCl₂, H₃BO₃ and NaOH as the raw materials, and *N,N*-dimethylformamide nitrate ionic liquid as the solvent. The porous MgBO₂(OH) microspheres exhibited a specific surface area of 57.22 m² g⁻¹, 82.4% of which had a diameter within the range of 4.0–6.0 μm. The subsequent mild thermal conversion (600 °C, 12.0 h) gave rise to the hierarchical porous Mg₂B₂O₅ microspheres with high crystallinity and a specific surface area of 24.20 m² g⁻¹. The synergistic effect of the hydrophilic surfaces of the MgBO₂(OH) nanostructures and the ionothermally confined self-organization co-contributed to the formation of the hierarchical porous MgBO₂(OH) and Mg₂B₂O₅ superstructures, which were employed as adsorbents for Congo red (CR) in simulated waste water. Both MgBO₂(OH) and Mg₂B₂O₅ superstructures exhibited good recyclability and reusability as high efficient adsorbents for dye removal after regeneration. The Langmuir isothermal model well interpreted the adsorption behavior of CR. The intra-particle diffusion model was also well fitted based on the kinetic data, indicating microsphere diffusion as the rate-limiting step. The maximum adsorption capacities, *q_m*, for CR onto the porous MgBO₂(OH) and Mg₂B₂O₅ superstructures, which were calculated from the Langmuir isothermal model, were 228.3 and 139.3 mg g⁻¹, respectively. The present ionothermally confined self-organization for the hierarchical porous MgBO₂(OH) and Mg₂B₂O₅ superstructures provide new insights into the material chemistry, as well as a controllable ionothermal route for hierarchical borate nanoarchitectures. In addition, these superstructures provide a new platform for dye adsorption, and other potential fields, such as heterogeneous catalysis.

Received 13th July 2014
Accepted 4th September 2014

DOI: 10.1039/c4ta03580a

www.rsc.org/MaterialsA

1. Introduction

Three-dimensional (3D) hierarchical micro-/nanostructured materials, self-assembled or self-organized by one-dimensional (1D) and two-dimensional (2D) building blocks, have attracted widespread attention due to their unique size- and morphology-dependent properties as well as novel applications, which make them increasingly practical.^{1–5} Among the multitude of 1D nanostructures or 1D nanostructured building blocks

constructed from hierarchical metal oxides, carbonates, and silicates, 1D magnesium borate nanostructures (*e.g.* Mg₂B₂O₅ nanowires,^{6–8} nanorods^{9,10} and whiskers,^{11–13} MgB₄O₇ nanowires,¹⁴ Mg₃B₂O₆ nanotubes¹⁵) have been significantly considered because of their excellent performances, when used as reinforcements in wide band gap semiconductors,⁶ electronic ceramics,¹⁴ antiwear additives,¹⁶ and plastics or aluminum/magnesium matrix alloys.¹⁷ As a matter of fact, in addition to the traditional high temperature techniques, such as chemical vapor deposition (CVD)^{6,9,10,14,15} and molten salt synthesis (MSS),^{18–20} for anhydrous 1D magnesium borate nanoarchitectures, hydrated and anhydrous 1D magnesium borate nanorods/nanowires/nanowhiskers have also been synthesized by hydrothermal synthesis^{8,21–23} or thermal conversions based on hydrothermal systems (HTC).^{12,24,25}

Templated hydrothermal or solvothermal synthesis is widely used for hierarchical nanostructure fabrications,^{2,26,27} but there

^aDepartment of Chemical Engineering, Qufu Normal University, Shandong 273165, China. E-mail: zhuwancheng@tsinghua.org.cn; Fax: +86-10-62772051; Tel: +86-537-4453130

^bBeijing Key Laboratory of Green Chemical Reaction Engineering and Technology, Department of Chemical Engineering, Tsinghua University, Beijing 100084, China. E-mail: zhang-qiang@mails.tsinghua.edu.cn

† Electronic supplementary information (ESI) available. See DOI: 10.1039/c4ta03580a

are technical bottlenecks for the impurity introduction and the inevitable structural collapse during the post-treatments for template removal. The temperature range for liquid water (0–100 °C) is relatively narrow, which limits the applications of hydrothermal synthesis for the reactions requiring lower or higher temperatures.²⁸ Whereas, solvothermal synthesis using organic solvents as media might suffer from the relatively low solubility of the inorganic reactants, as well as the potential security issues because organic solvents are toxic, flammable, and even explosive.²⁹ Therefore, it is highly desirable to seek alternative solvents that possess tunable and versatile solvent properties with easy disposal of the templates, as well as a facile, green and reliable synthesis of inorganic materials.

Ionic liquids (ILs), entirely consisting of ions, have attracted considerable attention because of their distinct physical and chemical properties, such as low melting points (below 100 °C), excellent thermal stability, negligible vapor pressure, and wide temperature range for dissolving both organic and inorganic compounds.³⁰ ILs have been extensively exploited as competitive alternatives for traditional solvents in numerous fields, such as catalysis, separation and electrochemistry.^{28,31} Nowadays, although many inorganic materials with novel morphologies and unique properties, including novel porous carbon,¹ hematite,³² and lithium iron phosphate,³³ have been produced *via* ILs-mediated or ionothermal synthesis, investigations are still required for such booming domain both in controllable synthesis and intrinsic mechanism. To date, there are very few reports on the ionothermal synthesis of borate nanostructures, including hierarchical borate superstructures. If the aforementioned 1D magnesium borates can be self-organized into 3D hierarchical and even porous superstructures, their dispersion in a polymer/metal/ceramic matrix would be greatly improved, and their applications could be further broadened to other areas, such as water treatment, catalysis and energy storage.

Recently, 3D flower-like $\text{Mg}_3\text{B}_2\text{O}_6$ microspheres assembled by nanosheets were synthesized *via* a poly(vinylpyrrolidone) (PVP)-assisted precipitation reaction and subsequent calcination (650 °C, 4.0 h).³⁴ Whereas, the mesoporous $2\text{MgO}\cdot\text{B}_2\text{O}_3$ microspheres with very low crystallinity were fabricated *via* a similar precipitation process followed by calcination (500 °C, 4.0 h) using sodium dodecyl sulfate (SDS) as a template.³⁵ Further enhancing the applications of magnesium borates is still a difficult issue and acquiring 3D hierarchical magnesium borate superstructures with relatively high crystallinity and porous structures is a great challenge.

In our previous work, 1D $\text{Mg}_2\text{B}_2\text{O}_5$ nanowhiskers^{12,24,25} were obtained based on the controllable hydrothermal formation of the $\text{MgBO}_2(\text{OH})$ nanowhiskers.^{21,36} Herein, we report for the first time our latest investigation on the facile ionothermal synthesis of hierarchical porous $\text{MgBO}_2(\text{OH})$ superstructures, followed by a subsequent thermal conversion which led to the formation of hierarchical porous $\text{Mg}_2\text{B}_2\text{O}_5$ superstructures; the possible formation mechanism is discussed. Moreover, both the as-obtained hierarchical porous $\text{MgBO}_2(\text{OH})$ and $\text{Mg}_2\text{B}_2\text{O}_5$ superstructures were evaluated to be novel recyclable adsorbents for toxic organic chemicals, such as Congo Red (CR), from simulated waste water.

2. Results and discussion

2.1. Ionothermal synthesis of hierarchical $\text{MgBO}_2(\text{OH})$ superstructures

The pre-prepared $[\text{DMFH}]^+\text{NO}_3^-$ ILs were employed as the medium for ionothermal synthesis. Fig. 1 shows the composition, profile, and size distribution of the ionothermal product synthesized at 150 °C for 12.0 h. As shown (Fig. 1(a)), all the diffraction peaks of the XRD pattern were readily indexed to those of the standard monoclinic $\text{MgBO}_2(\text{OH})$ (JCPDS no. 39-1370), and no other peak for impurities were detected. Notably, the pure crystal phase of the present ionothermal product was the same as that of the $\text{MgBO}_2(\text{OH})$ nanowhiskers derived from the hydrothermal synthesis; however, the strongest diffraction peak was located at $2\theta = 33.76^\circ$ for the corresponding plane ($\bar{1}21$). This was different from the generally strongest diffraction peak that corresponds to the (200) plane, which is parallel to the longitudinal direction, and it is also the preferential growth direction for $\text{MgBO}_2(\text{OH})$ nanowhiskers.^{21,36} The crystallite size D_{200} , calculated using the Debye-Scherrer equation, was 12.3 nm, indicating the approximate size perpendicular to the (200) planes, *i.e.* along the latitudinal direction of the 1D $\text{MgBO}_2(\text{OH})$ nanostructures.

The typical SEM image demonstrates the ionothermal products of hierarchical porous $\text{MgBO}_2(\text{OH})$ superstructures, containing a multitude of constitutional 1D nanobuilding blocks or subunits. The superstructures showed a uniform microspherelike profile and a narrow diameter distribution (Fig. 1(b)); 82.4% of the as-obtained superstructures had a diameter within the range of 4.0–6.0 μm (Fig. 1(b₁)). Moreover, some porous microspheres exhibited remarkable inner cavities within the spherical body, which are denoted as the yellow dotted-circle areas. The high-magnification SEM images (Fig. 1(c)) clearly reveal that the as-synthesized $\text{MgBO}_2(\text{OH})$ superstructures consisted of a large number of randomly stacked short tiny 1D nanofloccules or nanorods, whereas profound spherical profiles and distinct cavities were observed on the peripheral surfaces of the microspheres. The constitutional 1D nanorods had a length of less than 1.0 μm , which is considerably shorter than the previous hydrothermally obtained nanowhiskers at 240 °C for 18.0 h.^{21,36} In addition, both the low-magnification (Fig. 1(d)) and high-magnification TEM images, corresponding to the local surface (Fig. 1(d₁)) or the group of 1D subunits segregated from the bulk because of the ultrasonication applied during the course of sample preparation (Fig. 1(d₂)), reconfirmed the as-obtained microspheres of hierarchical porous superstructures. Such hierarchical porous superstructures with a well-defined spherical profile were significantly different from the agglomerated urchinlike spherical $\text{MgBO}_2(\text{OH})$ clusters.²³

2.2. Thermal conversion for hierarchical $\text{Mg}_2\text{B}_2\text{O}_5$ superstructures

The thermal decomposition property of the $\text{MgBO}_2(\text{OH})$ superstructures was evaluated by simultaneously recording the thermogravimetric-differential scanning calorimetric (TG-DSC) curves, as shown in Fig. 2. The sample mass decreased at a slow

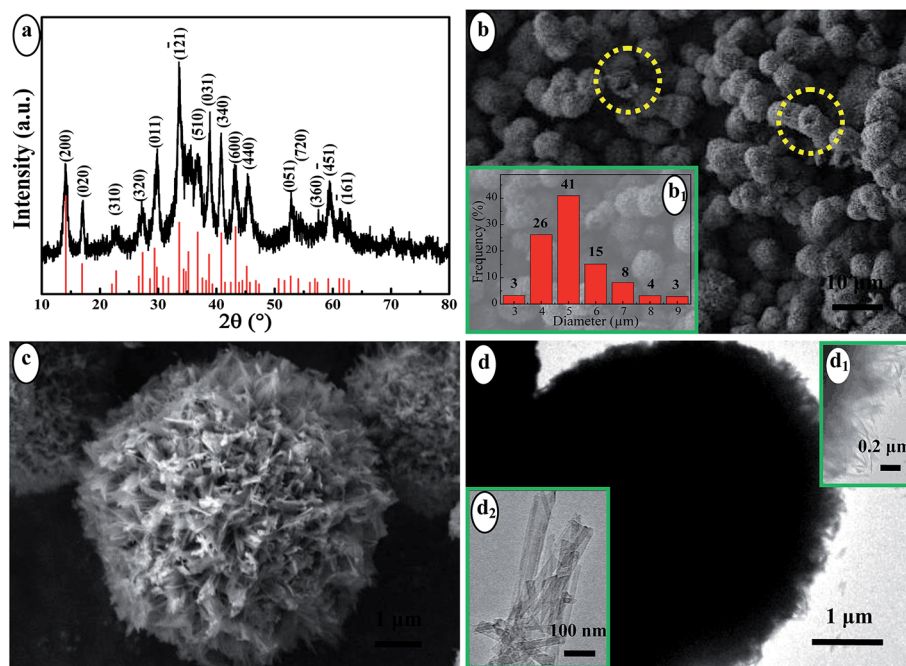
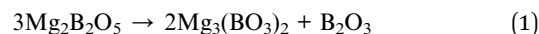


Fig. 1 XRD pattern (a), SEM (b and c) and TEM (d, d₁ and d₂) images of the hierarchical porous MgBO₂(OH) microspheres ionothermally synthesized at 150 °C for 12.0 h. The vertical lines in (a) indicate the standard pattern of monoclinic MgBO₂(OH) (JCPDS no. 39-1370). The inset (b₁) shows the size distribution of the MgBO₂(OH) microspheres.

rate below 295 °C, at a relatively faster rate between 295 and 440 °C, at a significantly faster rate between 440 and 595 °C, at a slightly slower rate between 650 and 800 °C, and thereafter remained almost constant. The gradual mass decrease before 440 °C was attributed to the elimination of physically absorbed water and the residual ILs³⁷ that were absorbed onto and inside the porous superstructures. The subsequent mass loss of 10.4% between 440 and 595 °C was similar to the theoretical weight loss (10.7%) for the conversion of MgBO₂(OH) to Mg₂B₂O₅.⁹ Notably, there was also a slightly slow rate of mass loss from 650 to 800 °C, which might be ascribed to the partial conversion of Mg₂B₂O₅ to Mg₃(BO₃)₂, as follows:^{12,25}



The final decomposition temperature (595 °C) of the MgBO₂(OH) superstructures was lower than that of the MgBO₂(OH) nanowhiskers (620 °C),²⁵ whereas considerably lower than that of natural szaibelyite (MgBO₂(OH), 700 °C),³⁸ because of the small size effect. The simultaneously recorded DSC curve exhibited a broad endothermic peak between 440 and 595 °C due to the dehydration of the structural water from MgBO₂(OH) superstructures. The slightly endothermic effect between 595 and 650 °C should be associated with the partial decomposition of Mg₂B₂O₅ to Mg₃(BO₃)₂. In particular, there emerged a sharp exothermic peak between 650 and 680 °C due to the recrystallization of Mg₂B₂O₅,³⁸ which was also consistent with our previous work.²⁵

Fig. 3 shows the composition, profile and size distribution of the calcined product derived from the thermal conversion of the ionothermally-synthesized MgBO₂(OH) superstructures at 600 °C for 12.0 h at a heating rate of 5 °C min⁻¹. As shown in Fig. 3(a), each diffraction peak in the XRD pattern could be assigned to that of the triclinic Mg₂B₂O₅ standard (JCPDS no. 73-2232). The crystallinity of the as-obtained Mg₂B₂O₅ superstructures was relatively lower than the triclinic Mg₂B₂O₅ nanowhiskers that were prepared by calcining MgBO₂(OH) nanowhiskers in the absence of NaCl at 650–700 °C for 2.0 h,²⁴ but considerably higher than the mesoporous 2MgO·B₂O₃ microspheres.³⁵ The as-calcined superstructures had hierarchical porous structures with a well preserved profile of MgBO₂(OH) microspheres (Fig. 3(b)). There were cavities within the body of the porous microspheres, which is denoted by the yellow dash-dotted-line circles areas in

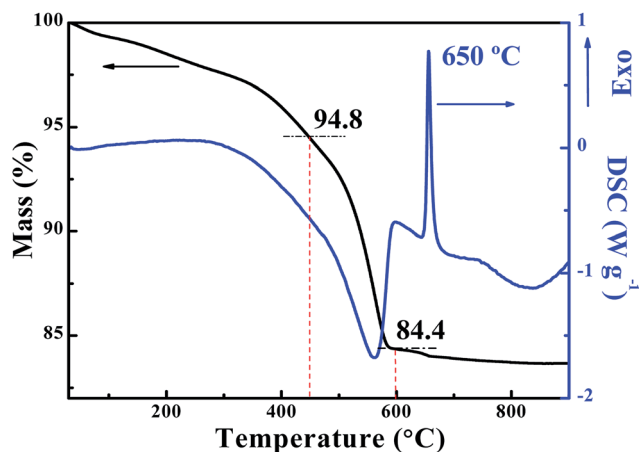


Fig. 2 TG-DSC curves of the hierarchical porous MgBO₂(OH) superstructures ionothermally synthesized at 150 °C for 12.0 h.

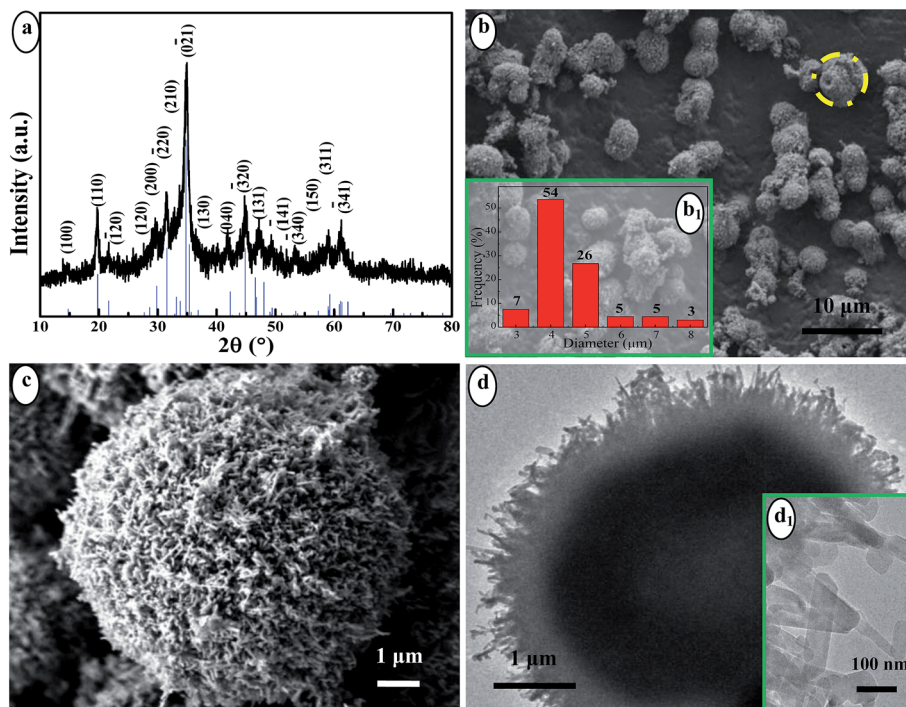


Fig. 3 XRD pattern (a), SEM (b and c) and TEM (d and d₁) images of the Mg₂B₂O₅ superstructures calcined at 600 °C for 12.0 h (heating rate: 5 °C min⁻¹). The vertical lines in (a) indicate the standard pattern of triclinic Mg₂B₂O₅ (JCPDS no. 73-2232). The inset b₁ shows the size distribution of the Mg₂B₂O₅ superstructures.

Fig. 3(b). In addition, the size distribution (Fig. 3(b₁)) indicated that *ca.* 80% of the Mg₂B₂O₅ superstructures had a diameter within the range of 3.0–5.0 μm, which is relatively smaller than that of the ionothermally synthesized MgBO₂(OH) superstructures due to the dehydration. Moreover, the high-magnification SEM image (Fig. 3(c)) clearly reveal that the Mg₂B₂O₅ superstructures are composed of numerous tiny nanorods with a smaller size due to pore shrinkage during the course of thermal conversion compared to the constitutional nanorods within the MgBO₂(OH) superstructures. The TEM images (Fig. 3(d and d₁)) reconfirmed the as-calcined hierarchical porous superstructures of a well-defined spherical profile and constitutional tiny nanorods.

To better understand the thermal decomposition properties of the ionothermally synthesized MgBO₂(OH) superstructures, the calcination temperature, time and heating rate were tuned within the range of 600–700 °C, 2.0–8.0 h and 2–10 °C min⁻¹, respectively, to investigate the corresponding effect on the calcined products. As shown in Fig. S1,† the pure phase of triclinic Mg₂B₂O₅ (JCPDS no. 73-2232) was available, when calcined at 600 °C for various growth durations and at various heating rates. However, when calcined at higher temperature, such as 700 °C, a mixture of triclinic Mg₂B₂O₅ and Mg₃(BO₃)₂ (JCPDS no. 33-0858) were obtained.

2.3. Hierarchical porous structures within the MgBO₂(OH) and Mg₂B₂O₅ microspheres

Typical nitrogen adsorption–desorption isotherms were recorded to examine the porous structures within the MgBO₂(OH)

and Mg₂B₂O₅ microspheres, as shown in Fig. 4. The sorption isotherms of both MgBO₂(OH) (Fig. 4(a)) and Mg₂B₂O₅ (Fig. 4(b)) superstructures demonstrated the type IV isotherm with H3-type hysteresis loops according to the Brunauer–Deming–Deming–Teller classification, revealing the dominant narrow slit-shaped mesopores within the superstructures.³⁹ Whereas, the sorption isotherms of the Mg₂B₂O₅ microspheres displayed a narrower hysteresis loop at relatively high pressure of $P/P_0 = 0.8–1.0$, indicating the constitutional macropores are present within the calcined loose superstructures. In addition, the pore size distribution (PSD) indicated that the MgBO₂(OH) superstructures contained few mesopores and abundant macropores. Moreover, the Mg₂B₂O₅ microspheres contained more textural mesopores with pore diameters within the range of 3–5 nm due to the dehydration during the thermal conversion process. Taking into consideration the size of the constitutional tiny nanorods within the superstructures, the mesopores should be due to the N₂ sorption measurements (MgBO₂(OH)) or previous dehydration (Mg₂B₂O₅), whereas the macropores should be mainly derived from the organization of the nanorod building blocks within the superstructures. In particular, the Mg₂B₂O₅ microspheres contained more macropores than the MgBO₂(OH) microspheres due to the thermal conversion, which can be with the SEM observations (Fig. 1(c) and 2(c)).

The hierarchical porous MgBO₂(OH) microspheres exhibited a specific surface area of 57.22 m² g⁻¹, a pore volume of 0.32 cm³ g⁻¹, and an average pore radius of 1.85 nm. The specific surface area was considerably larger than that of the mesoporous 2MgO·B₂O₃ microspheres (53.03 m² g⁻¹).³⁵ After thermal conversion, the as-obtained hierarchical porous

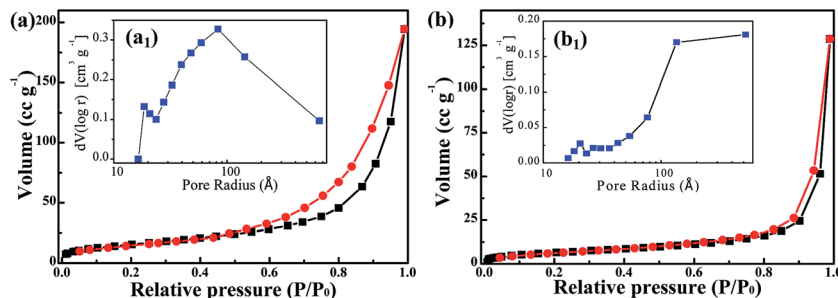
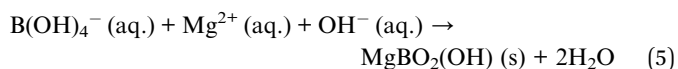
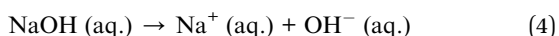
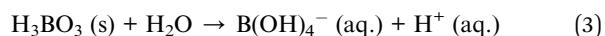
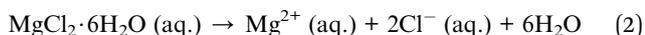


Fig. 4 Nitrogen adsorption–desorption isotherms (a and b) and the corresponding pore radius distribution curves (a_1 and b_1) of the $\text{MgBO}_2(\text{OH})$ (a and a_1) and $\text{Mg}_2\text{B}_2\text{O}_5$ (b and b_1) superstructures.

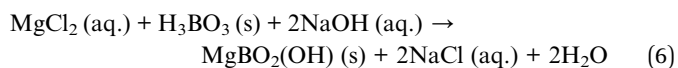
$\text{Mg}_2\text{B}_2\text{O}_5$ microspheres demonstrated a specific surface area of $24.20 \text{ m}^2 \text{ g}^{-1}$, a pore volume of $0.20 \text{ cm}^3 \text{ g}^{-1}$ and an average pore radius of 2.06 nm. Apparently, the specific surface area was slightly lower than that of the porous $\text{MgBO}_2(\text{OH})$ microsphere precursor. However, the hierarchical porous $\text{MgBO}_2(\text{OH})$ and $\text{Mg}_2\text{B}_2\text{O}_5$ microspheres with high crystallinity have potential applications for adsorption.

2.4. Formation mechanism of hierarchical porous $\text{MgBO}_2(\text{OH})$ and $\text{Mg}_2\text{B}_2\text{O}_5$ superstructures

The ionothermal treatment played a key role in the formation of the $\text{MgBO}_2(\text{OH})$ and $\text{Mg}_2\text{B}_2\text{O}_5$ superstructures. The resulting white slurry containing NaOH , $\text{MgCl}_2 \cdot 6\text{H}_2\text{O}$ and H_3BO_3 could not completely dissolve into the ILs but was thoroughly water soluble. Taking into consideration the phase change before and after the ionothermal treatment, the corresponding ionic reactions can be written as follows:



The overall ionothermal chemical conversion can be expressed as follows:



This is different from the previous hydrothermal formation of the $\text{MgBO}_2(\text{OH})$ nanowhiskers, which was derived from the hydrothermal conversion of the amorphous intermediate, *i.e.* the room temperature coprecipitate, $\text{Mg}_7\text{B}_4\text{O}_{13} \cdot 7\text{H}_2\text{O}$.³⁶ In addition to the water derived from the reactant $\text{MgCl}_2 \cdot 6\text{H}_2\text{O}$ (eqn (2)), there was also some water formed according to eqn (5), even under the deliberately designed ionothermal conditions.

To better understand the intrinsic mechanism, the effects of the ionothermal temperature and time on the product were

investigated, as shown in Fig. S2 and S3,[†] respectively. When ionothermally treated at 70°C , no solid state product was available. When ionothermally treated at various temperatures above 100°C for 12.0 h (Fig. S2[†]), the products were all confirmed to be pure phase $\text{MgBO}_2(\text{OH})$ (JCPDS no. 39-1370), and the crystallinity of the product increased with increasing temperature in the range of 100 – 180°C . After the ionothermal treatment at 120°C , the product exhibited poor crystallinity and a short nanorod-like morphology (Fig. S2(a_1 and b_1))[†], which was attributed to the initial anisotropic growth of $\text{MgBO}_2(\text{OH})$ in the ILs, and was considerably similar to the hydrothermal formation of $\text{MgBO}_2(\text{OH})$ at 100 – 120°C with a rudimentary 1D morphology.⁴⁰ With the temperature increasing to 140°C , the product became quasi-spherical $\text{MgBO}_2(\text{OH})$ assembly with a non-uniform PSD (Fig. S2(a_2 and c))[†]. When the temperature was increased to 150, 160 and further 180°C , the product was confirmed to be comprised of uniform hierarchical porous microspheres (Fig. 1), which evolved into porous microspheres with a relatively broad PSD (Fig. S2(a_3 and d))[†] and further transformed to be quasi-spherical disassembled units because of the significantly high temperature ionothermal treatment (Fig. S2(a_4 and e))[†].

When ionothermally treated at 150°C for various durations, similar growth phenomena were observed. The crystallinity increased with time from 6.0 to 16.0 h. After 6.0 h of the ionothermal treatment, the low crystallinity and rudimentary spherical $\text{MgBO}_2(\text{OH})$ assemblies (Fig. S3(a_1 and b))[†] were obtained. After being ionothermally treated for 8.0 h (Fig. S3(a_2 and c))[†], 10.0 h (Fig. S3(a_3 and d))[†] and 12.0 h (Fig. 3), the products became increasingly uniform with a distinct spherical profile and hierarchical porous structures (denoted as the red dotted-circle region in Fig. S3(d))[†] and yellow dash-dotted-line circle regions in Fig. 1(b)). However, when ionothermally treated for a longer time, such as 16.0 h, the hierarchical porous microspheres disassembled, resulting in remarkable spindle or bundle-like $\text{MgBO}_2(\text{OH})$ architectures containing 1D nanostructures with higher aspect ratios (Fig. S3(a_4 and e))[†], which originated from the side-by-side oriented growth of the $\text{MgBO}_2(\text{OH})$ nanowhiskers along the (200) planes.⁴⁰ The phenomena of the disassembled growth of the hierarchical porous $\text{MgBO}_2(\text{OH})$ superstructures in the case of over ionothermal treatment, *e.g.* at temperatures higher than 150°C for a time longer than 12.0 h, was considerably similar to that

observed in the hydrothermal formation of the laminar rhombic $\text{Ca}_4\text{B}_{10}\text{O}_{19} \cdot 7\text{H}_2\text{O}$ superstructures.⁴¹

Based on the abovementioned experimental results, a formation mechanism of the hierarchical porous $\text{MgBO}_2(\text{OH})$ and $\text{Mg}_2\text{B}_2\text{O}_5$ superstructures was proposed, as illustrated in Fig. 5. Firstly, the water derived from the reactant led to spherical water bubbles or reservoirs due to surface tension, this reduced the overall energy within the ILs. Such water bubbles favored and continuously trapped the dissolved Mg^{2+} , $\text{B}(\text{OH})_4^-$ and OH^- ions from the deposited solid reactants, resulting in a milky-white and quasi-w/o microemulsion system under constant magnetic stirring. Secondly, with increasing ionothermal temperature, the trapped Mg^{2+} , $\text{B}(\text{OH})_4^-$ and OH^- ions within the reservoirs reacted with each other, producing the original $\text{MgBO}_2(\text{OH})$ nanostructures with a basic 1D nanorod-like morphology with the concomitant dissolution of the reactants. Thirdly, with the progressing ionothermal treatment, the newly dissolved ions continuously migrated to the reservoirs, not only serving as the requisite nutrients for heterogeneous or homogeneous nucleation but also considerably pushing the pre-formed nanorods to move out towards the interfaces between the water and ILs. Fourthly, the hydrophilic effect of the nanorod surfaces stabilized the ionothermally confined, self-organization of the $\text{MgBO}_2(\text{OH})$ nanorods, and thus brought about the uniform hierarchical porous $\text{MgBO}_2(\text{OH})$ superstructures with a microsphere-like profile. Finally, subsequent mild thermal conversion obtained the final formation of the hierarchical porous $\text{Mg}_2\text{B}_2\text{O}_5$ superstructures with the well preserved microsphere-like profile of precursor.

2.5. Synergistic effect of hydrophilic surfaces and ionothermal confined self-organization

The hydrophilic effect and ionothermal confined self-organization is believed to be responsible for the formation of the present $\text{MgBO}_2(\text{OH})$ and $\text{Mg}_2\text{B}_2\text{O}_5$ hierarchical porous superstructures. Nevertheless, the 1D $\text{MgBO}_2(\text{OH})$ nanorods could not fully grow due to the confinement of water bubbles within

the ILs compared to those grown at the same temperature and time under hydrothermal conditions. As confirmed from Fig. S4,† with decreasing volume ratios of ILs/water from 8/1 to 3/1 to 2/1 and to 0/1, the aspect ratio of the 1D $\text{MgBO}_2(\text{OH})$ nanostructures increased. Simultaneously, with the increasing amount of water, the self-organization of the 1D building blocks became increasingly blurred and even disappeared. Consequently, an optimal amount of water bubbles are crucial for the ionothermal confined self-organization for the present hierarchical porous $\text{MgBO}_2(\text{OH})$ superstructures. More amount of water was favorable for the growth of high aspect ratio $\text{MgBO}_2(\text{OH})$ nanostructures rather than the corresponding ionothermal confined self-organization. In other words, the $\text{MgBO}_2(\text{OH})$ nanostructures exhibited hydrophilic surfaces, which favored their preferential growth into high aspect ratio nanostructures in a hydrous environment.

To date, the roles of the ILs during the synthesis of inorganic materials were viewed as a solvent,⁴² template,⁴³ direction agent,⁴⁴ capping agent, stabilizing agent,³³ or modifying agent.⁴⁵ To gain more insight into the specific role of the present ILs in the ionothermal self-organization of the hierarchical porous $\text{MgBO}_2(\text{OH})$ microspheres, a series of control experiments were performed using DMF, DMA, miscible liquids (*i.e.* HNO_3 and DMF), as well as the liquid recovered from the former ionothermal treatment as solvents (Fig. S5†). All the products (Fig. S5(a–d)†) were confirmed to be of $\text{MgBO}_2(\text{OH})$ phase (XRD patterns not shown here), but only the liquid recovered from the former ionothermal synthesis promoted the formation of $\text{MgBO}_2(\text{OH})$ microspheres (Fig. S5(d)†), indicating that the present ILs are essential for the ionothermal self-organization of the hierarchical porous superstructures, as well as for the relatively better recyclability of the ILs. Actually no solid state product was obtained, when the liquid collected from the previously heat treated DMF (150 °C, 12.0 h) was used as the solvent. This revealed that the decomposition product of DMF (150 °C, 12.0 h) could not favor the formation of the $\text{MgBO}_2(\text{OH})$ phase, including the corresponding self-organization.

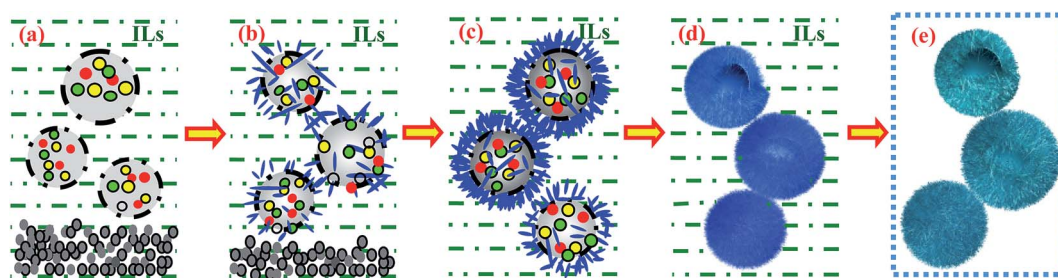


Fig. 5 Proposed mechanism for the formation of hierarchical $\text{MgBO}_2(\text{OH})$ and $\text{Mg}_2\text{B}_2\text{O}_5$ superstructures by ionothermal–thermal conversion synthesis. (a) Water originating from the reactant led to spherical water bubbles or reservoirs within the ILs, which favored and continuously trapped the dissolved Mg^{2+} , $\text{B}(\text{OH})_4^-$ and OH^- ions from the deposited solid reactants; (b) with increasing temperature, Mg^{2+} , $\text{B}(\text{OH})_4^-$ and OH^- ions reacted with each other, producing the original basic 1D nanorod-like $\text{MgBO}_2(\text{OH})$ nanostructures with the concomitant dissolution of the reactants; (c) the newly dissolved ions continuously migrated into the reservoirs, serving as the requisite nutrients for heterogeneous or homogeneous nucleation and pushing the pre-formed nanorods to move out towards the interfaces between the water and ILs; (d) hydrophilic effect of the nanorod surfaces stabilized the ionothermal confined self-organization of the nanorods to obtain the uniform hierarchical porous $\text{MgBO}_2(\text{OH})$ microspheres; (e) mild thermal conversion gave rise to the final hierarchical porous $\text{Mg}_2\text{B}_2\text{O}_5$ microspheres (● – Mg^{2+} , ● – $\text{B}(\text{OH})_4^-$, ● – OH^- , ▬ – $\text{MgBO}_2(\text{OH})$, ▬ – $\text{Mg}_2\text{B}_2\text{O}_5$).

Therefore, the ILs probably served as a liquid solvent that could form a stable quasi-w/o microemulsion system, when it contained an applicable amount of water bubbles, which would further create a confinement effect during the ionothermal formation of MgBO₂(OH) microspheres. This was significantly similar to the effect of ILs in the synthesis of Bi₂S₃ nanostructures reported by Jiang *et al.*⁴⁶ Thus, it should be the synergistic effect of the hydrophilic surfaces of the MgBO₂(OH) nanostructures and the ionothermal confined self-organization that co-contributed to the formation of the hierarchical porous MgBO₂(OH) superstructures. However, an excess of ionothermal treatment, *i.e.* ionothermal treatment at excessively high temperatures (higher than 160 °C) for an excessively long time (longer than 16.0 h), caused lower stability of the ILs. This further affected the formation of the quasi-w/o microemulsion system and restrained the further ionothermal confined self-organization for the hierarchical porous superstructures.

2.6. Dye adsorption on hierarchical porous MgBO₂(OH) and Mg₂B₂O₅ superstructures

The as-synthesized hierarchical porous MgBO₂(OH) and Mg₂B₂O₅ superstructures were employed as the adsorbents for CR removal from simulated waste water. CR is a secondary diazo dye and a representative organic pollutant commonly used in the cotton textile, wood pulp, and paper industries, with a characteristic UV-vis adsorption at *ca.* 496 nm. As shown in Fig. 6(a), both porous superstructures exhibited satisfactory adsorption rates because the C_t/C_0 value for the adsorption of CR onto MgBO₂(OH) and Mg₂B₂O₅ superstructures was relatively constant within 40 and 140 min, respectively. The removal efficiency of CR from the simulated solution rapidly approached *ca.* 94.21% and 90.89% within 120 min for MgBO₂(OH) and Mg₂B₂O₅ porous microspheres, respectively, and remained relatively constant thereafter. The adsorption rate of the MgBO₂(OH) porous microspheres was faster than that of the Mg₂B₂O₅ porous microspheres; the variation of the adsorption capacity with the contact time is shown in Fig. 6(b). The adsorption capacity of the MgBO₂(OH) porous microspheres at any instant, *i.e.* q_t , was also higher than that of the Mg₂B₂O₅ porous microspheres, almost within the entire adsorption time range. The faster adsorption rate as well as the higher

adsorption capacity for CR onto the MgBO₂(OH) porous microspheres can be attributed to the correspondingly larger specific surface area, pore volume and specific surface properties of the porous superstructures.

An analysis of the adsorption isotherm is essential to understand the adsorption mechanism of the distribution of adsorbate molecules between a liquid and adsorbent according to a series of assumptions related to the heterogeneity/homogeneity of adsorbents, the type of coverage, and the possibility of interactions among the adsorbate molecules.⁴⁷ The Langmuir and Freundlich isotherm models are typical mathematical models that have been widely employed for the investigations of the adsorption mechanisms. The former model was based on the assumption that all sorption sites on the adsorbent are identical and energetically equivalent, and the latter is based on the fact that the adsorption is a multilayer adsorption on heterogeneous surfaces, which is reversible. The Langmuir isotherm indicates monolayer coverage, whereas the Freundlich isotherm reveals no restriction. Mathematically, the Langmuir and Freundlich models can be expressed as eqn (7) and (8), respectively, as follows:

$$q_e = \frac{q_m b c_e}{1 + b c_e} \quad (7)$$

$$q_e = k_f c_e^{1/n} \quad (8)$$

where q_e is the amount of CR adsorbed on the adsorption surfaces at equilibrium (mg g^{-1}), q_m is the theoretical maximum adsorption capacity (mg g^{-1}), b is the coefficient related to the energy of adsorption, and c_e is the concentration of the CR in solution at equilibrium (mg L^{-1}). For the Freundlich model, k_f and $1/n$ are constants related to the adsorption capacity at a unit concentration and adsorption intensity, respectively.

The experimental data for the adsorption of CR was fitted with both models, which is presented in Fig. 7. When the data are fitted with the Langmuir model, the correlation coefficients R^2 of the hierarchical porous MgBO₂(OH) and Mg₂B₂O₅ superstructures were both 0.9903 (Table S1[†]), which are considerably higher than those of the hierarchical porous MgBO₂(OH) and Mg₂B₂O₅ superstructures fitted with the Freundlich models

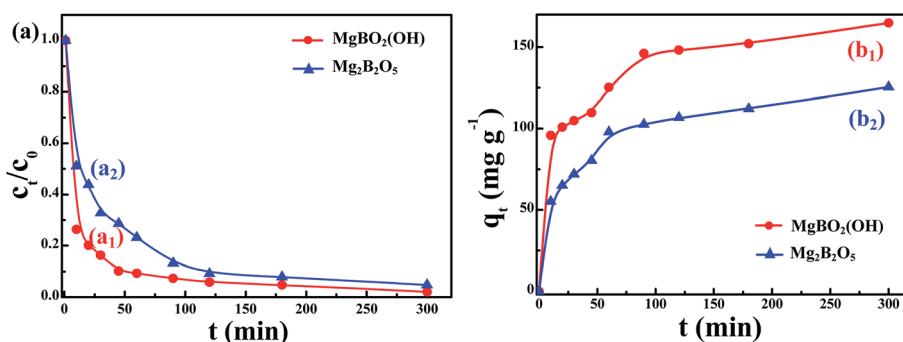


Fig. 6 Adsorption rate (a) and capacity (b) of the MgBO₂(OH) (a₁ and b₁) and Mg₂B₂O₅ (a₂ and b₂) superstructures for CR removal as a function of the contact time with an initial concentration of 50 mg L^{-1} .

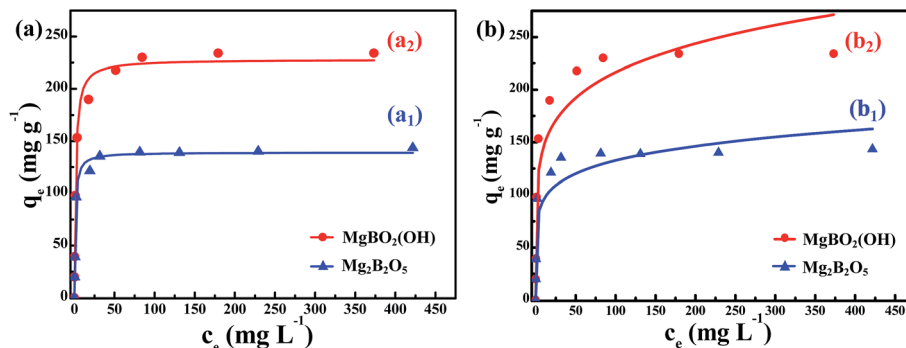


Fig. 7 Adsorption isotherms of CR onto the hierarchical porous $\text{MgBO}_2(\text{OH})$ (a_2 and b_2) and $\text{Mg}_2\text{B}_2\text{O}_5$ (a_1 and b_1) superstructures, fitted with the Langmuir model (a_1 and a_2) and Freundlich (b_1 and b_2) model, respectively.

(0.8890 and 0.8766, respectively) (Table S1†). Thus, compared with the Freundlich model, the Langmuir model presented a satisfactory fitting result, which reveals that the adsorption of CR on the as-obtained hierarchical porous $\text{MgBO}_2(\text{OH})$ and $\text{Mg}_2\text{B}_2\text{O}_5$ superstructures was a monolayer adsorption process. In other words, the sites that had been occupied by the adsorbate molecules could not undergo further adsorption and there were no strong interactions among the adsorbate molecules. The maximum adsorption capacities of CR adsorption onto the hierarchical porous $\text{MgBO}_2(\text{OH})$ and $\text{Mg}_2\text{B}_2\text{O}_5$ superstructures derived from the Langmuir isotherm model were 228.3 and 139.3 mg g^{-1} , respectively (Table S1†).

The present prominent removal efficiency of CR was believed to be associated with the specific hierarchical porous structures within the microspheres, and the maximum adsorption capacities for CR for various adsorbents were also compared, which is listed in Table 1. Both the $\text{MgBO}_2(\text{OH})$ and $\text{Mg}_2\text{B}_2\text{O}_5$ porous microspheres exhibit relatively higher adsorption abilities than some traditional oxides, such as Fe_3O_4 microspheres,⁴⁸ urchin-like $\alpha\text{-Fe}_2\text{O}_3$,⁴⁹ and $\alpha\text{-Fe}_2\text{O}_3$ hollow structures.⁵⁰ However, the q_m did not proportionally increase with increasing specific surface area of the adsorbents, indicating probable additional electrostatic interactions between CR and the adsorbents, which also played a significant role in determining the adsorption efficiency. In addition, the q_m of the $\text{MgBO}_2(\text{OH})$ microspheres was much higher than that of the $\text{Mg}_2\text{B}_2\text{O}_5$ microspheres, probably because of the larger surface area and interactions between $-\text{OH}$ and CR molecules. Moreover, the q_m of the $\text{MgBO}_2(\text{OH})$ microspheres was even larger than that of the hollow nest-like $\alpha\text{-Fe}_2\text{O}_3$ spheres⁵¹ and hierarchical spindle-like $\gamma\text{-Al}_2\text{O}_3$ (ref. 52) with significantly larger specific surface areas, reconfirming that the specific surface area was not the most important factor for determining the adsorption capacity. Notably, the q_m of the $\text{MgBO}_2(\text{OH})$ microspheres was smaller than that of the MgO (111) nanoplates⁵³ and CdO cauliflower-like nanostructures⁵⁴ because of the relatively smaller specific surface area of the former, and the strong electrostatic interactions between the latter adsorbents with the employed dye species. Overall, the adsorption test confirmed the as-obtained porous $\text{Mg}_2\text{B}_2\text{O}_5$, especially $\text{MgBO}_2(\text{OH})$ microspheres, to be an ideal adsorbent candidate for treatment of water containing CR. In addition to

the specific surface area of the porous structures, the electrostatic interactions between the present hierarchical porous microspheres and the employed CR dye should be responsible for the satisfactory adsorption performance. However, further investigations are needed to obtain a better understanding.

To further evaluate the adsorption mechanism of CR on the hierarchical $\text{MgBO}_2(\text{OH})$ and $\text{Mg}_2\text{B}_2\text{O}_5$ superstructures, three typical kinetic models were adopted to interpret the adsorption data, in which the pseudo-first-order and pseudo-second-order kinetic models were mostly used. The pseudo-first-order kinetic model (*i.e.* Lagergren kinetic model) is commonly employed for studying adsorption in aqueous solutions, which is depicted as follows:

$$\log(q_e - q_t) = \log q_e - \frac{k_1}{2.303} t \quad (9)$$

where q_e and q_t (mg L^{-1}) are the amounts of CR adsorbed at equilibrium and at time t (min), respectively, k_1 is the rate constant (min^{-1}) and t (min) is the contact time between the adsorbent and adsorbate.

Whereas, the pseudo-second-order kinetic model could be expressed as follows:

$$\frac{t}{q_t} = \frac{1}{k_2 q_e^2} + \frac{t}{q_e} \quad (10)$$

where k_2 is the pseudo-second-order rate constant ($\text{g mg}^{-1} \text{min}^{-1}$), q_e is the amount of CR adsorbed at equilibrium (mg g^{-1}), q_t is the amount of CR adsorbed at any time (mg g^{-1}), and t is the time (min).

When the pseudo-first-order kinetic model was employed, the values of the adsorption constant k_1 were calculated from the plot of $\log(q_e - q_t)$ vs. t (Fig. 8(a)) for $\text{MgBO}_2(\text{OH})$ and $\text{Mg}_2\text{B}_2\text{O}_5$, which is listed in Table S2.† The fitted correlation coefficients R^2 for the adsorption of CR onto the $\text{MgBO}_2(\text{OH})$ and $\text{Mg}_2\text{B}_2\text{O}_5$ microspheres were 0.6192 and 0.9244, respectively. Whereas, both $q_{e,\text{calc1}}$ values for the $\text{MgBO}_2(\text{OH})$ and $\text{Mg}_2\text{B}_2\text{O}_5$ microspheres calculated using the pseudo-first-order kinetic model were 26.57 and 57.59 g mg^{-1} , respectively, showing significant variation from the corresponding experimental values, $q_{e,\text{exp}}$. Both the correlation coefficients R^2 and the remarkable gap between the calculated $q_{e,\text{calc1}}$ values and the corresponding experimental $q_{e,\text{exp}}$ values suggested that the fitted results by the pseudo-first-

Table 1 Comparison of the maximum adsorption capacities (q_m , mg g^{-1}) for CR on various adsorbents

Adsorbents	S_{BET} ($\text{m}^2 \text{g}^{-1}$)	q_m (mg g^{-1})	References
Eucalyptus wood saw dust	0.3742	31.25	55
Fe_3O_4 microspheres	71.5	42.55	48
Hierarchical urchin-like $\alpha\text{-Fe}_2\text{O}_3$ nanostructures	69	66	49
$\gamma\text{-Al}_2\text{O}_3/\text{Ni}_{0.5}\text{Zn}_{0.5}\text{Fe}_2\text{O}_4$ microfibers	118.3	75.5	56
$\alpha\text{-Fe}_2\text{O}_3$ hollow structures	32.9	93.55	50
Ca-bentonite	—	107.41	57
Hierarchical porous $\text{Mg}_2\text{B}_2\text{O}_5$ superstructures	24.20	139.3	This work
Hollow nest-like $\alpha\text{-Fe}_2\text{O}_3$ spheres	152.42	160	51
Hierarchical spindle-like $\gamma\text{-Al}_2\text{O}_3$	149	176.7	52
Porous Mn/ Fe_3O_4 nanowires	45.4	180	58
Hierarchical porous $\text{MgBO}_2(\text{OH})$ superstructures	57.22	228.3	This work
MgO (111) nanoplates	198	303	53
CdO cauliflower-like nanostructure	104	588.2	54

order kinetic model were not satisfactory. Therefore, the pseudo-first-order kinetic model could not explain the adsorption kinetics. In other words, the physical adsorption, which was based on the adsorption force through van der Waals force, π - π force, and hydrogen bonding between the adsorbent and adsorbate, is not the rate-limiting step.

Comparatively, when the pseudo-second-order kinetic model was employed, a linear plot of t/q_t against t was obtained (Fig. 8), and the q_e , and k_2 values were also obtained (Table S2†). Both correlation coefficients R^2 were higher than 0.99, which indicated that the adsorption process of CR on the hierarchical $\text{MgBO}_2(\text{OH})$ or $\text{Mg}_2\text{B}_2\text{O}_5$ superstructures can be more appropriately interpreted using the pseudo-second-order kinetic model rather than the pseudo-first-order kinetic model. The $q_{e,\text{calc}2}$ values for the adsorption of CR onto the hierarchical $\text{MgBO}_2(\text{OH})$ or $\text{Mg}_2\text{B}_2\text{O}_5$ superstructures, calculated from the pseudo-second-order kinetic model were 99.01 and 97.09 g mg^{-1} , which are similar to the corresponding experimental values for the concentration of adsorbate $q_{e,\text{exp}}$ obtained at equilibrium. Clearly, the $q_{e,\text{calc}2}$ values derived from the pseudo-second-order kinetic model were significantly closer to the corresponding $q_{e,\text{exp}}$ values than the $q_{e,\text{calc}1}$ values that originated from the pseudo-first-order kinetic model. This reveals that the rate-limiting step for CR adsorption onto the hierarchical $\text{MgBO}_2(\text{OH})$ and $\text{Mg}_2\text{B}_2\text{O}_5$ superstructures should be

chemical adsorption, which is related to the valence forces by sharing or exchanging electrons between the adsorbent and adsorbate. However this needs further investigation of adsorption thermodynamics.

In order to better understand the adsorption mechanism, the intra-particle diffusion model was further investigated in order to verify the possible transportation of CR molecules into the pores of the $\text{MgBO}_2(\text{OH})$ and $\text{Mg}_2\text{B}_2\text{O}_5$ microspheres. The model is described as follows:

$$q_t = k_{\text{dif}}\sqrt{t} + c \quad (11)$$

where k_{dif} is the intra-particle diffusion rate constant ($\text{mg g}^{-1} \text{h}^{-1/2}$), and c is the intercept (mg g^{-1}), which represents the thickness of the boundary layer. Larger the intercept c , greater is the contribution of the surface adsorption in the rate controlling step. If intra-particle diffusion is the rate-limiting step, the plot of the adsorbate uptake q_t vs. the square root of time t ($\text{h}^{1/2}$) would exhibit a linear relationship. As shown in Fig. 9, the experimental data were divided into two steps, which were fitted to the intra-particle diffusion model because of the difference in the rate of mass transfer at the initial and final stages of adsorption. Such deviation of the straight lines fitted using the origin software indicated that pore diffusion was not the only rate-controlling step,⁵⁹ similar to the results of CR diffusion into the pores of eucalyptus wood saw dust.⁵⁵

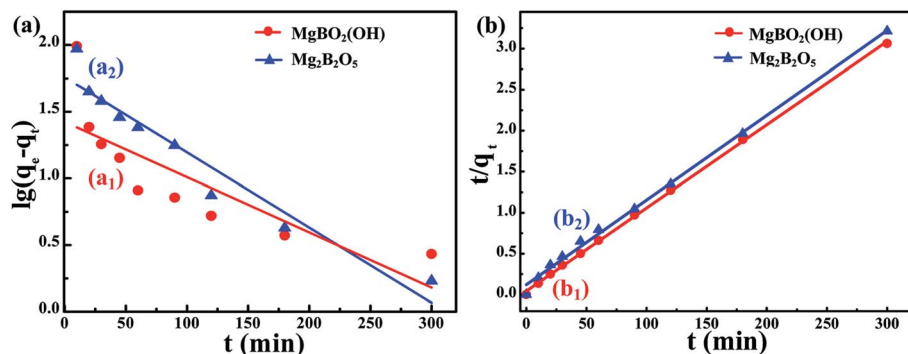


Fig. 8 Pseudo-first-order (a) and pseudo-second-order (b) kinetic plots of CR (50 mg L^{-1}) adsorption on the hierarchical porous $\text{MgBO}_2(\text{OH})$ (a_1 and b_1) and $\text{Mg}_2\text{B}_2\text{O}_5$ (a_2 and b_2) superstructures.

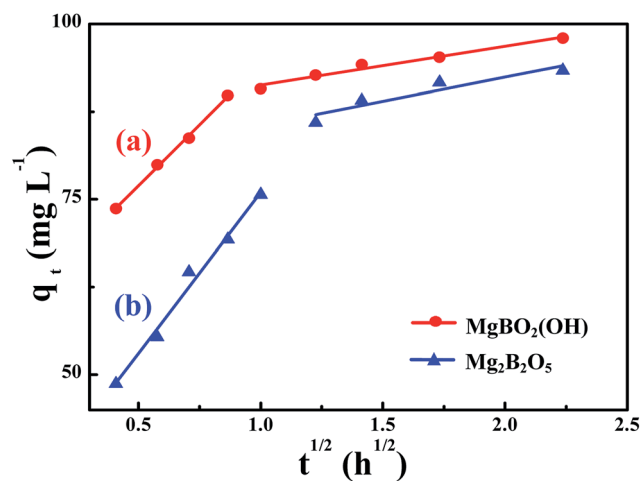


Fig. 9 Intra-particle diffusion model for the adsorption of CR (50 mg L⁻¹) on the hierarchical porous MgBO₂(OH) (a) and Mg₂B₂O₅ (b) superstructures.

The first stage in the diffusion model was the mass transfer of adsorbate molecules from the bulk solution to the adsorbent surface, or to put it simply, the instantaneous stage was attributed to the macropores diffusion. In contrast, the second linear portion was the intra-particle diffusion to the mesopores within the MgBO₂(OH) and Mg₂B₂O₅ superstructures. To determine the rate-controlling step within the intra-particle diffusion, an attempt was made to confirm the rate constant k_{dif} from the intra-particle diffusion plots (Fig. 9), which is listed in Table S3.† By comparing the values of k_{dif} for two stages, the high $k_{\text{dif}1}$ and low $k_{\text{dif}2}$ values were obtained from the macropores and mesopores diffusion stages, respectively. This revealed that the rate-limiting step was diffusion in mesopores. It was obtained from the intercepts (c_1 , c_2) of the fitted lines that the boundary effects played a significant role in the entire diffusion process than macroporous diffusion.

2.7. Recyclability and reusability of the MgBO₂(OH) and Mg₂B₂O₅ superstructures as adsorbents

The recyclability and reusability of the adsorbents are quite important for the practical applications. After adsorption, the originally white porous MgBO₂(OH) and Mg₂B₂O₅ superstructures became red due to the adsorption of CR. By calcination to regenerate the adsorbents, the red MgBO₂(OH) and Mg₂B₂O₅ superstructures containing CR turned again to white. The regenerated superstructures were used for the second and third time adsorption. As shown in Fig. S6(a and b),† after calcination (400 °C, 2.0 h) to eliminate the adsorbed CR, the profile and porous structure of the MgBO₂(OH) and Mg₂B₂O₅ microspheres were significantly retained. The good preservation of the porous superstructures greatly contributed to their comparable adsorption rate performance (Fig. S6(c and d)†), when calcined and regenerated for the second and third time. The adsorption performance of the regenerated adsorbents did not significantly decrease during the subsequent second and third time adsorption. When employed in the third circle, the removal

efficiency of CR by MgBO₂(OH) porous superstructures within 120 min was confirmed to be 91.0%, showing only a decrease of 3.2% compared to the newly prepared MgBO₂(OH) superstructures. Simultaneously, the removal efficiency of CR by the second time regenerated Mg₂B₂O₅ reached 86.5%. This shows that the as-obtained hierarchical porous MgBO₂(OH) and Mg₂B₂O₅ superstructures are highly efficient adsorbents for dye removal with good recyclability and reusability.

3. Conclusion

Uniform hierarchical porous MgBO₂(OH) superstructures with a microsphere-like profile were synthesized *via* facile ionothermal synthesis (150 °C, 12.0 h) using MgCl₂, H₃BO₃ and NaOH as the raw materials, and *N,N*-dimethylformamide nitrate ionic liquid as the solvent. The as-synthesized hierarchical porous MgBO₂(OH) superstructures exhibited a specific surface area of 57.22 m² g⁻¹, 82.4% of which had a diameter within the range of 4.0–6.0 μm. The mild thermal conversion of the MgBO₂(OH) superstructures (600 °C, 12.0 h) gave rise to the hierarchical porous Mg₂B₂O₅ superstructures with high crystallinity and a specific surface area of 24.20 m² g⁻¹. The synergistic effect of the hydrophilic surfaces of the MgBO₂(OH) nanostructures and the ionothermal confined self-organization also contributed to the formation of the hierarchical porous MgBO₂(OH) and Mg₂B₂O₅ superstructures, which were used as adsorbents for Congo red (CR) from simulated waste water. The results showed that the hierarchical porous MgBO₂(OH) superstructures exhibited outstanding adsorption capacity compared to the other adsorbents reported in the literature, and also higher than the presently studied Mg₂B₂O₅ superstructures. The maximum adsorption capacities q_m for CR on the porous MgBO₂(OH) and Mg₂B₂O₅ superstructures were 228.3 and 139.3 mg g⁻¹, respectively. Isothermal modeling showed that the Langmuir isothermal model better interpreted the adsorption behavior of CR on the MgBO₂(OH) and Mg₂B₂O₅ superstructures, and the intra-particle diffusion model also well fitted to the kinetic data. This suggests that diffusion within the mesopores is the rate-limiting step. The calcination and regeneration of the adsorbents containing CR and its reuse for adsorption confirmed that the as-obtained MgBO₂(OH) and Mg₂B₂O₅ superstructures are highly efficient for dye removal with good recyclability and reusability. The present ionothermal confined self-organization for hierarchical porous MgBO₂(OH) and Mg₂B₂O₅ superstructures provides new insights into the chemistry of these materials, as well as a controllable ionothermal route to obtain hierarchical porous metal borate nanoarchitectures, and a new platform for dye adsorption and other potential fields, such as heterogeneous catalysis.

4. Experimental section

4.1. Synthesis of *N,N*-dimethylformamide (DMF) nitrate ionic liquid

All reagents were of analytical grade and used as received. The *N,N*-dimethylformamide nitrate ionic liquid ([DMFH]⁺NO₃⁻) was obtained by neutralization of DMF with a dilute HNO₃

solution (2.0 M) in a low temperature water bath (*ca.* 5 °C), and the dilute acid was added dropwise with maintaining a volume ratio of DMF : HNO₃ = 1.1 : 1.0, similar to that reported elsewhere.³⁷ The resulting colorless liquid was transferred into a rotary evaporator for the removal of water, DMF, and HNO₃ residues, and the as-obtained light yellow liquid was collected and purified by vacuum drying at 60 °C for 12.0 h, producing the final light yellow ILs.

4.2. Ionothermal synthesis of hierarchical porous MgBO₂(OH) superstructures

In a typical procedure, a certain amount of NaOH powder was dissolved in 30.0 mL of the as-synthesized ILs until the pH was adjusted to *ca.* 7.0 under constant magnetic stirring at room temperature, resulting in a white emulsion. Subsequently, 4.066 g (0.02 mol) MgCl₂·6H₂O and 1.855 g (0.03 mol) H₃BO₃ were sequentially added to the emulsion, which could not completely dissolve into the ILs. After stirring for another 10.0 min, the resulting slurry was transferred into a Teflon-lined stainless steel autoclave. The autoclave was sealed, heated to 150.0 °C and kept in an isothermal state for 12.0 h with a heating rate of 5.0 °C min⁻¹. After the abovementioned ionothermal conversion, the autoclave was naturally cooled to room temperature. The as-obtained precipitate was filtered, washed with deionized (DI) water, rinsed three times with anhydrous absolute ethanol, and finally dried at 60.0 °C for 24.0 h for characterization. To investigate the influence of temperature and time on the ionothermal formation of the products, the temperature and time were tuned within the range of 120–180 °C, and 6.0–16.0 h, respectively. To investigate the impact of DI water on the ionothermal process, the volume ratio of ILs to DI water was altered as 8 : 1, 3 : 1, 2 : 1, and 0 : 1. In addition, to ascertain the role of ILs on the formation of the products, the same reactant system was also conducted using alternative solvents, such as DMF, dimethylamine (DMA), DMF/HNO₃, or the liquid collected after the above normal ionothermal reaction (150 °C, 12.0 h) as the medium, with the other conditions kept same.

4.3. Thermal conversion for hierarchical porous Mg₂B₂O₅ superstructures

The former as-synthesized hierarchical MgBO₂(OH) superstructures were transferred into a porcelain boat located in a horizontal tube furnace, which was heated to 600–700 °C at a heating rate of 5 °C min⁻¹ and kept under isothermal conditions for 2.0–12.0 h, leading to the formation of hierarchical porous Mg₂B₂O₅ superstructures. After calcination, the product was naturally cooled to room temperature for further characterization. To investigate the effect of the calcination parameters, the temperature, heating rate and time were tuned within 600–700 °C, 2–10 °C min⁻¹, and 2.0–12.0 h, respectively, with the other conditions unchanged.

4.4. Hierarchical porous superstructures as adsorbents for dye removal

Hierarchical porous MgBO₂(OH) and Mg₂B₂O₅ superstructures were employed as adsorbents for the removal of Congo Red (CR)

from simulated waste water. Specifically, MgBO₂(OH) (20.0 mg) and Mg₂B₂O₅ (20.0 mg) were added to the individually prepared CR containing solutions (40.0 mL), respectively, under vigorous magnetic stirring at room temperature, keeping the initial concentration and adsorption time within the range of 10.0–500.0 mg L⁻¹ and 10–300 min, respectively. The adsorption rate of CR by MgBO₂(OH) and Mg₂B₂O₅ superstructures was evaluated by the ratio of C_t/C_0 , where C_0 and C_t represent the concentration of CR (mg L⁻¹) at time 0 and at certain intervals during the adsorption process, respectively. In addition, to study the kinetics of adsorption, the adsorption in the CR solution with an initial concentration of 50.0 mg L⁻¹ was monitored. The adsorption capacity of the adsorbents for CR was calculated using the following equation:

$$q_t = \frac{(c_0 - c_t)V}{m} \quad (12)$$

$$q_e = \frac{(c_0 - c_e)V}{m} \quad (13)$$

where q_t is the adsorption capacity at time t (mg g⁻¹), and q_e is the equilibrium adsorption capacity (*i.e.* the adsorbed mass of CR onto the adsorbents MgBO₂(OH) or Mg₂B₂O₅ superstructures under the equilibrium conditions, mg g⁻¹), V is the volume of the employed CR solution (L), C_0 and C_e represent the initial and equilibrium concentrations of the CR solution (mg g⁻¹), respectively, C_t indicates the concentration of the CR solution at any time t , and m is the mass of the introduced adsorbents MgBO₂(OH) or Mg₂B₂O₅ (g).

4.5. Evaluation of the recyclability and reusability of MgBO₂(OH) and Mg₂B₂O₅ superstructures

After adsorption, the red MgBO₂(OH) and Mg₂B₂O₅ superstructures containing the adsorbed CR were collected by centrifugation and regenerated by calcination at 400 °C for 2.0 h at a heating rate of 2 °C min⁻¹ in air for the decomposition and elimination of CR; whereas the profile and porous structure of MgBO₂(OH) and Mg₂B₂O₅ were significantly preserved. The regenerated adsorbents were employed for second and third adsorptions to evaluate the recyclability and reusability of the porous MgBO₂(OH) and Mg₂B₂O₅ superstructures.

4.6. Characterization

The crystal structure of the samples were identified by X-ray powder diffraction (XRD, MiniFlex600, Rigaku, Japan) with Cu K_α radiation ($\lambda = 1.5406 \text{ \AA}$) and a fixed power source (40.0 kV, 15.0 mA). The morphology and microstructure of the samples were examined by field emission scanning electron microscopy (SEM, JSM 7401F, JEOL, Japan, at 3.0 kV) and high resolution transmission electron microscopy (TEM, JEM-2010, JEOL, Japan, at 120.0 kV). The size distribution of the as-synthesized superstructures was estimated by directly measuring about 100 particles from the typical SEM images. The thermal decomposition behavior was determined using a thermal-gravimetric analyzer operating in the range of (TGA, Netzsch STA 409C, Germany) 30 to 950 °C in air at a heating rate of 10.0 °C min⁻¹.

The porous structure of the samples was characterized by the N₂ adsorption–desorption isotherms, which were measured at 77 K using a chemisorption–physisorption analyzer (Autosorb-1-C, Quantachrome, Boynton Beach, FL, USA) after the samples had been degassed at 300 °C for 1.0 h, and the pore sizes were evaluated from the N₂ desorption isothermal using the Barrett–Joyner–Halenda (BJH) method. To evaluate the adsorption properties, after the adsorption had been performed for the designated time, the as-collected filtrate was quantitatively analyzed and the absorbance was determined using a UV-vis spectrophotometer (UV-756 CRT, Shanghai Yoke Instrument and Meter Co., LTD, China).

Acknowledgements

This work was supported by the National Natural Science Foundation of China (no. 21276141), the State Key Laboratory of Chemical Engineering, China (no. SKL-ChE-12A05). The authors thank Dr Wei Qi of School of Chemistry and Chemical Engineering, Qufu Normal University, China, for the helpful discussion. The authors are also much obliged to the reviewers for the constructive suggestions on the great improvement of the work.

References

- Z. L. Xie, R. J. White, J. Weber, A. Taubert and M. M. Titirici, *J. Mater. Chem.*, 2011, **21**, 7434–7442.
- Y. Li, Z. Y. Fu and B. L. Su, *Adv. Funct. Mater.*, 2012, **22**, 4634–4667.
- M. Q. Zhao, Q. Zhang, J. Q. Huang and F. Wei, *Adv. Funct. Mater.*, 2012, **22**, 675–694.
- N. D. Petkovich and A. Stein, *Chem. Soc. Rev.*, 2013, **42**, 3721–3739.
- W. Q. Wu, Y. F. Xu, H. S. Rao, H. L. Feng, C. Y. Su and D. B. Kuang, *Angew. Chem., Int. Ed.*, 2014, **53**, 4816–4821.
- Y. Li, Z. Y. Fan, J. G. Lu and R. P. H. Chang, *Chem. Mater.*, 2004, **16**, 2512–2514.
- X. Tao and X. Li, *Nano Lett.*, 2008, **8**, 505–510.
- W. Zhu, X. Zhang, L. Xiang and S. Zhu, *Nanoscale Res. Lett.*, 2009, **4**, 724–731.
- E. M. Elssfah, A. Elsanousi, J. Zhang, H. Song and C. Tang, *Mater. Lett.*, 2007, **61**, 4358–4361.
- B. S. Xu, T. B. Li, Y. Zhang, Z. X. Zhang, X. G. Liu and J. F. Zhao, *Cryst. Growth Des.*, 2008, **8**, 1218–1222.
- W. Zhu, Q. Zhang, L. Xiang and S. Zhu, *CrystEngComm*, 2011, **13**, 1654–1663.
- W. Zhu, Q. Zhang, L. Xiang and S. Zhu, *Cryst. Growth Des.*, 2011, **11**, 709–718.
- W. Zhu, R. Wang, S. Zhu, L. Zhang, X. Cui, H. Zhang, X. Piao and Q. Zhang, *ACS Sustainable Chem. Eng.*, 2014, **2**, 836–845.
- R. Z. Ma, Y. Bando and T. Sato, *Appl. Phys. Lett.*, 2002, **81**, 3467–3469.
- R. Z. Ma, Y. Bando, D. Golberg and T. Sato, *Angew. Chem., Int. Ed.*, 2003, **42**, 1836–1838.
- Y. Zeng, H. B. Yang, W. Y. Fu, L. Qiao, L. X. Chang, J. J. Chen, H. Y. Zhu, M. H. Li and G. T. Zou, *Mater. Res. Bull.*, 2008, **43**, 2239–2247.
- S. H. Chen, P. P. Jin, G. Schumacher and N. Wanderka, *Compos. Sci. Technol.*, 2010, **70**, 123–129.
- T. Kitamura, K. Sakane and H. Wada, *J. Mater. Sci. Lett.*, 1988, **7**, 467–469.
- K. Sakane, H. Wada, T. Kitamura and M. Suzue, *Gypsum Lime*, 1991, **235**, 16–21.
- K. Sakane, T. Kitamura, H. Wada and M. Suzue, *Adv. Powder Technol.*, 1992, **3**, 39–46.
- W. Zhu, L. Xiang, X. Zhang and S. Zhu, *Mater. Res. Innovations*, 2007, **11**, 188–192.
- B. S. Xu, T. B. Li, Y. Zhang, Z. X. Zhang, X. G. Liu and J. F. Zhao, *Cryst. Growth Des.*, 2008, **8**, 1218–1222.
- L. Kumari, W. Li, S. Kulkarni, K. Wu, W. Chen, C. Wang, H. Vannoy and R. Leblanc, *Nanoscale Res. Lett.*, 2009, **5**, 149–157.
- W. Zhu, Q. Zhang, L. Xiang, F. Wei, X. Sun, X. Piao and S. Zhu, *Cryst. Growth Des.*, 2008, **8**, 2938–2945.
- W. Zhu, L. Xiang, Q. Zhang, X. Zhang, L. Hu and S. Zhu, *J. Cryst. Growth*, 2008, **310**, 4262–4267.
- M. Titirici, R. White, C. Falco and M. Sevilla, *Energy Environ. Sci.*, 2012, **5**, 6796–6822.
- H. Colfen and M. Antonietti, *Angew. Chem., Int. Ed.*, 2005, **44**, 5576–5591.
- Z. Ma, J. Yu and S. Dai, *Adv. Mater.*, 2010, **22**, 261–285.
- C. Reichardt, *Org. Process Res. Dev.*, 2007, **11**, 105–113.
- S. A. Forsyth, J. M. Pringle and D. R. MacFarlane, *Aust. J. Chem.*, 2004, **57**, 113–119.
- X. Zhang, X. Zhang, H. Dong, Z. Zhao, S. Zhang and Y. Huang, *Energy Environ. Sci.*, 2012, **5**, 6668–6681.
- G. Gao, Q. Zhang, K. Wang, H. Song, P. Qiu and D. Cui, *Nano Energy*, 2013, **2**, 1010–1018.
- F. Teng, M. Chen, G. Li, Y. Teng, T. Xu, S. Mho and X. Hua, *J. Power Sources*, 2012, **202**, 384–388.
- A. Chen, P. Gu and Z. Ni, *Mater. Lett.*, 2012, **68**, 187–189.
- A. Chen, P. Gu and J. Hu, *Adv. Mater. Res.*, 2012, **486**, 260–264.
- W. Zhu, L. Xiang, T. He and S. Zhu, *Chem. Lett.*, 2006, **35**, 1158–1159.
- J. Huang, G. Baker, H. Luo, K. Hong, Q. Li, N. Bjerrum and S. Dai, *Green Chem.*, 2006, **8**, 599–602.
- X. D. Xie and L. B. Liu, *Borate Minerals*, Science Press, Beijing, 1965, p. 54.
- R. Chen, J. Yu and W. Xiao, *J. Mater. Chem. A*, 2013, **1**, 11682–11690.
- W. Zhu, S. Zhu and L. Xiang, *CrystEngComm*, 2009, **11**, 1910–1919.
- W. Zhu, X. Wang, X. Zhang, H. Zhang and Q. Zhang, *Cryst. Growth Des.*, 2011, **11**, 2935–2941.
- A. Imanishi, S. Gonsui, T. Tsuda, S. Kuwabata and K. Fukui, *Phys. Chem. Chem. Phys.*, 2011, **13**, 14823–14830.
- T. L. Greaves and C. J. Drummond, *Chem. Soc. Rev.*, 2013, **42**, 1096–1120.
- L. Wang, L. X. Chang, L. Q. Wei, S. Z. Xu, M. H. Zeng and S. L. Pan, *J. Mater. Chem.*, 2011, **21**, 15732–15740.

- 45 Z. Zhu, X. Li, Y. Zeng, W. Sun, W. Zhu and X. Huang, *J. Phys. Chem. C*, 2011, **115**, 12547–12553.
- 46 J. Jiang, S. Yu, W. Yao, H. Ge and G. Zhang, *Chem. Mater.*, 2005, **17**, 6094–6100.
- 47 J. Zhou, S. Yang and J. Yu, *Colloids Surf., A*, 2011, **379**, 102–108.
- 48 I. D. Mall, V. C. Srivastava, N. K. Agarwal and I. M. Mishra, *Colloids Surf., A*, 2005, **264**, 17–28.
- 49 J. B. Fei, Y. Cui, J. Zhao, L. Gao, Y. Yang and J. B. Li, *J. Mater. Chem.*, 2011, **21**, 11742–11746.
- 50 J. S. Wu, Y. H. Du, J. S. Wang, K. L. Huang, H. Y. Li and B. X. Liu, *J. Mater. Chem. A*, 2013, **1**, 9837–9847.
- 51 Z. Wei, R. Xing, X. Zhang, S. Liu, H. Yu and P. Li, *ACS Appl. Mater. Interfaces*, 2013, **5**, 598–604.
- 52 W. Cai, J. Yu and M. Jaroniec, *J. Mater. Chem.*, 2010, **20**, 4587–4594.
- 53 J. C. Hu, Z. Song, L. F. Chen, H. J. Yang, J. L. Li and R. Richards, *J. Chem. Eng. Data*, 2010, **55**, 3742–3748.
- 54 A. Tadjarodi, M. Imani and H. Kerdari, *J. Nanostructure Chem.*, 2013, **3**, 1–8.
- 55 V. S. Mane and P. V. Vijay Babu, *J. Taiwan Inst. Chem. Eng.*, 2013, **44**, 81–88.
- 56 X. C. Yang, Z. Wang, M. X. Jing, R. J. Liu, L. N. Jin and X. Q. Shen, *Water, Air, Soil Pollut.*, 2014, **225**, 1–12.
- 57 L. Lian, L. Guo and C. Guo, *J. Hazard. Mater.*, 2009, **161**, 126–131.
- 58 H.-J. Cui, J.-W. Shi, B. Yuan and M.-L. Fu, *J. Mater. Chem. A*, 2013, **1**, 5902–5907.
- 59 T. K. Naiya, P. Chowdhury, A. K. Bhattacharya and S. K. Das, *Chem. Eng. J.*, 2009, **148**, 68–79.